

PAPER • OPEN ACCESS

## Highly efficient sequestration of aqueous lead on nanostructured calcite substrates



To cite this article: Matteo Barelli *et al* 2023 *Nanotechnology* **34** 365301

View the [article online](#) for updates and enhancements.

### You may also like

- [Biom mineralization: mineral formation by organisms](#)  
Lia Addadi and Steve Weiner
- [Functional adaptation of crustacean exoskeletal elements through structural and compositional diversity: a combined experimental and theoretical study](#)  
Helge-Otto Fabritius, Andreas Ziegler, Martin Friák et al.
- [Molecular dynamics simulation of the rotational order–disorder phase transition in calcite](#)  
Jun Kawano, Akira Miyake, Norimasa Shimobayashi et al.

# Highly efficient sequestration of aqueous lead on nanostructured calcite substrates

Matteo Barelli<sup>1</sup>, Santiago Casado<sup>2</sup>, Felix Cassin<sup>3</sup>, Carlos Pimentel<sup>4,7</sup>,  
Carlos M Pina<sup>5</sup>, Maria Caterina Giordano<sup>1</sup>,  
Francesco Buatier de Mongeot<sup>1,\*</sup>  and Enrico Gnecco<sup>6</sup> 

<sup>1</sup> Dipartimento di Fisica, Università di Genova, Via Dodecaneso 33, I-16136 Genova, Italy

<sup>2</sup> Facultad de Ciencia e Ingeniería en Alimentos, Universidad Técnica de Ambato, 180207 Ambato, Ecuador

<sup>3</sup> Department of Mechanical Engineering and Materials Science, University of Pittsburgh, Pittsburgh, United States of America

<sup>4</sup> Instituto Andaluz de Ciencias de la Tierra (CSIC-UGR). E-18100, Armilla, Granada, Spain

<sup>5</sup> Departamento de Mineralogía y Petrología, Universidad Complutense de Madrid, E-28040 Madrid, Spain, and Instituto de Geociencias (UCM-CSIC), E-28040 Madrid, Spain

<sup>6</sup> Marian Smoluchowski Institute of Physics, Jagiellonian University, 30-348 Krakow, Poland

E-mail: [giordano@fisica.unige.it](mailto:giordano@fisica.unige.it) and [buatier@fisica.unige.it](mailto:buatier@fisica.unige.it)

Received 9 March 2023, revised 26 May 2023

Accepted for publication 6 June 2023

Published 23 June 2023



CrossMark

## Abstract

Following defocused ion beam sputtering, large area highly corrugated and faceted nanoripples are formed on calcite (10.4) faces in a self-organized fashion. High resolution atomic force microscopy (AFM) imaging reveals that calcite ripples are defined by facets with highly kinked (11.0) and (2 $\bar{1}$ .12) terminations. *In situ* AFM imaging during the exposure of such modified calcite surfaces to PbCl<sub>2</sub> aqueous solution reveals that the nanostructured calcite surface promotes the uptake of Pb. In addition, we observed the progressive smoothing of the highly reactive calcite facet terminations and the formation of Pb-bearing precipitates elongated in registry with the underlying nanopattern. By SEM-EDS analysis we quantified a remarkable 500% increase of the Pb uptake rate, up to 0.5 atomic weight % per hour, on the nanorippled calcite in comparison to its freshly cleaved (10.4) surfaces. These results suggest that nanostructured calcite surfaces can be used for developing future systems for lead sequestration from polluted waters.

Supplementary material for this article is available [online](#)

Keywords: nanopatterning, ion beam sputtering, ion bombardment, metal sorption, water purification, atomic force microscopy

(Some figures may appear in colour only in the online journal)

<sup>7</sup> Present address: Université Grenoble Alpes, Université Savoie Mont Blanc, CNRS, IRD, Université Gustave Eiffel, ISTerre, 38000 Grenoble, France.

\* Author to whom any correspondence should be addressed.



Original content from this work may be used under the terms of the [Creative Commons Attribution 4.0 licence](#). Any further distribution of this work must maintain attribution to the author(s) and the title of the work, journal citation and DOI.

## 1. Introduction

Human population growth poses stress on the environment and it is responsible for the continued increase in water pollution. High concentrations of heavy metals (e.g. As, Cd, Pb, Hg, Zn, Co) in water can enter into the food chain and cause serious health problems in humans, as well as in animals and plants [1]. To reduce the amount of heavy metals in the environment, it has been proposed the use of some minerals to remove dissolved metal cations from polluted water [2–4].

For this purpose, minerals such as carbonates [2–6], phosphates [7], sulphates [8, 9] and clays [10–13] have been recognized to be very suitable materials. Furthermore, nanoconfinement of molecules and/or reactive chemical species in solids play a crucial role for tailoring chemical and physical properties, such as reaction rate, selectivity, and optoelectronic response [14–16]. In order to maximize surface interaction, the nanoscale tailoring of mineral surfaces is fundamental to use them in effective systems for sequestration of pollutants. In this respect, cost-effective approaches are required to achieve a functionalization of large-area surfaces suitable for environmental applications ranging from industrial waste purification to river water monitoring. In this vein, the production of self-organized and self-assembled nanopatterned materials represents a key strategy to create homogeneous structures over macroscopic areas, which permit, at the same time, control at multiple scales [17–23].

Self-organized ion beam sputtering of surfaces can be used to generate anisotropic patterns with controlled morphology at the nanoscale, and it represents a promising route for large-area nano-functionalization of minerals. Using this approach, highly ordered faceted nanorippled profiles have been already achieved on top of dielectric substrates by exploiting a nanoscale ion-induced wrinkling instability, which strongly enhances the degree of order and the vertical dynamic of the anisotropic nanopatterns [21]. These peculiar high aspect ratio nanopatterns have recently enabled a variety of large-area applications ranging from optoelectronics and biosensing to nanomechanics [22–27]. However, the effective nanopatterning of mineral surfaces is still an open issue since only a few experimental attempts have been performed so far [28], generally achieving shallow nanopatterns with no preferential orientation of their ridges and, therefore, with a low efficiency for contaminant sequestration.

Here we show a first example of high-aspect ratio mineral nano-template at the surface of calcite ( $\text{CaCO}_3$ ). Its peculiar wrinkled morphology, characterized by defined facets extends homogeneously over large area ( $\text{cm}^2$ ), it is a promising candidate for enhanced metal sequestration at the nanoscale. To investigate the contaminant sequestration capabilities of such a modified calcite surface we used atomic force microscopy (AFM). Since its invention, AFM turned into one of the most versatile techniques to investigate the reactivity of natural mineral surfaces at the nanoscale. *In situ* and *ex situ* AFM observations of those surfaces in contact with undersaturated and supersaturated aqueous solutions are allowing us to gain an unprecedented understanding of the way in which minerals interact with fluids [29]. Crystal growth, congruent and incongruent dissolution, incorporation of chemical species into crystal structures (i.e. solid solution formation), and leaching processes are some of the phenomena whose molecular-scale mechanisms can be now investigated by this technique [30]. Furthermore, the use of aqueous solutions containing organic molecules and nanoparticles permits to directly investigate processes such as adsorption on mineral terraces, inhibition of monostep motion and self-assembly of molecules on surfaces [31, 32]. In the context of the present work, the interaction of calcite with lead in aqueous solution

was already investigated using AFM on freshly cleaved crystals without artificial nanostructures [33–37]) Here we show enhanced Pb sequestration on relatively large areas of the abundant mineral calcite, which have been previously nanopatterned in a self-organised fashion with high aspect-ratio nanowrinkles to enhance their reactivity. Nanoscale resolved AFM measurements performed *in situ* within a flow cell allow us to monitor in real time the formation of anisotropic Pb-precipitates which are formed in registry with the highly reactive kinked nanopatterns. The *in situ* AFM results are complemented by *ex situ* scanning electron microscopy (SEM) microscopy and by *ex-situ* Scanning Electron Microscopy (SEM) microscopy and Energy Dispersive X-ray Spectrometry (EDS) elemental characterization of the local Pb uptake, which show that Pb sequestration is much faster on the nanostructured and faceted calcite substrate. Geochemical simulations support the experimental observations, indicating that hydrocerussite followed by cerussite are possibly the main Pb bearing mineral precipitates formed on calcite surfaces.

## 2. Results and discussion

Maskless defocused ion beam irradiation of calcite ( $\text{CaCO}_3$ ) was performed under grazing incidence conditions ( $\theta = 80^\circ$  with respect to the sample surface normal), directly exposing the freshly cleaved calcite (10.4) face to the action of the  $\text{Ar}^+$  ion beam, at an ion flux of  $260 \mu\text{A cm}^{-2}$  and an energy of 800 eV while keeping the sample holder at room temperature (more details on the experimental setup and experimental parameters are described in the Methods section). Under these ion irradiation conditions a slight temperature increase by few tens of degrees of the top surface layers is estimated to take place, which in combination with ion-induced ballistic energy transfer favours diffusion and recrystallization of the mobile surface adatoms [18, 21]. As shown in the AFM topography of figure 1(a), following ion irradiation of the pristine calcite substrate, large-area anisotropic ripple nanopatterns are effectively induced. The AFM topographies are measured in ambient conditions with the experimental setup described in the Methods section. Remarkably, the self-organized ion irradiation promotes the formation of high aspect-ratio nanoripples elongated parallel to the ion beam direction, and characterized by vertical dimension exceeding 100 nm, as highlighted by the AFM cross-section profile (figure 1(b)). The evolution of this peculiar high-aspect ratio nanopattern in the so called erosive regime can be attributed to the preferential sputtering of the mineral facets directly exposed to the ion beam incidence. Here the ion induced roughening mechanism is strongly boosted promoting ripples' growth [38]. The average ripples peak to valley height,  $h$ , reads about 92 nm, corresponding to a root mean square average (RMS) surface roughness of 33 nm. The dominant periodicity  $\Lambda$ , of the two main spatial modulations reads about 265 nm and 540 nm, as estimated from the first two peaks of the autocorrelation function of the AFM topography (figures 1(c)–(d) and from the 1D-PSD power spectral density described in

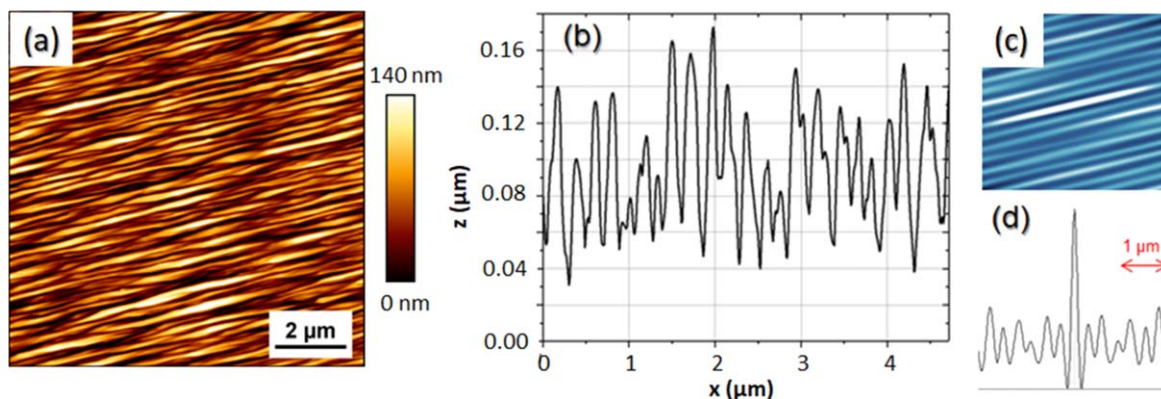


**Figure 1.** (a) AFM topography image of a rippled calcite (10.4) surface and (b) AFM cross-section profile of the same nanopattern extracted by the image shown in panel (a). (c) 2D autocorrelation pattern of the AFM image shown in panel (a) and (d) corresponding cross-section profile extracted through the center and perpendicular to the ripple elongation.

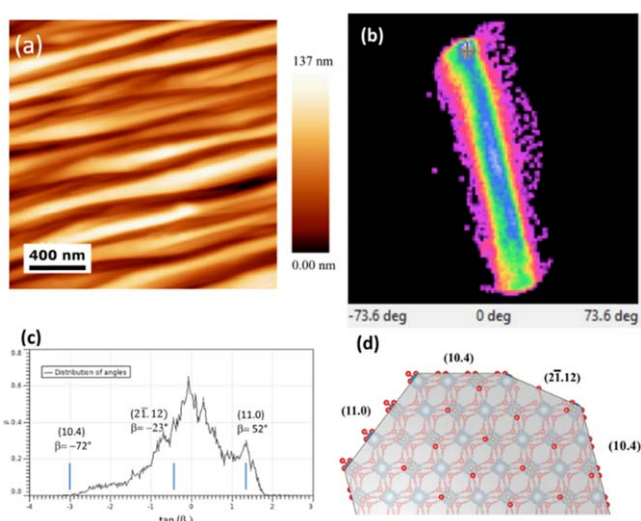


**Figure 2.** (a) AFM topography image of a rippled calcite (10.4) surface and (b) polar histogram of two-dimensional slope distribution of AFM topography of 1(a). (c) line profile of slope distribution orthogonal to ripple axis. (d) ball-stick model of calcite surface showing the structure of the possible predominant facets which define the ripples.

figure SI3 of supporting information (SI). These values are reflected in the very high average aspect ratio,  $h/\Lambda = 0.31$ , of the nanoripples by the steep slopes and by bunching of a high density of laterally correlated and kinked atomic steps. We have also estimated the minimum radii of curvature of the ripple crests and of the valley bottoms which respectively read 9.2 nm and 5.9 nm (at most), with the second value possibly influenced by convolution with the tip shape.

A more detailed and quantitative analysis of the high-resolution AFM topographies, performed in terms of facet slope distribution, is represented in figure 2(a). The two-dimensional histogram of the facet distribution (figure 2(b)) and the one-dimensional cut orthogonal to the ripple axis (figure 2(c)) allows to identify the predominant presence of specific (11.0) facets tilted at about  $52^\circ$  from the global plane, and bounding the ripple sides. A significant density of step bunching is also observed on the opposite side of the ripples (facets at negative angles reaching up to  $\beta = -72^\circ$ ).

Once measured the ripple slopes, an in-depth study of the calcite structure was performed. The ball-stick model shown in figure 2(d) allowed us to identify that to those slopes correspond to well defined crystal terminations, i.e. the (11.0) facets with a slope of  $52^\circ$  and the ( $2\bar{1}.12$ ) facets with a slope of  $-23^\circ$  with respect to the calcite (10.4) surface. Such facet terminations expose a high density of reactive kink sites [39, 40].

An issue to be stressed is that self-organized ion beam sputtering of a complex multicomponent mineral surface such as calcite not only leads to the formation of a periodic ripple pattern, but remarkably also leads to the formation of faceted terminations bound by reactive nanosteps. Previous reports on nanopatterning by ion beam sputtering of amorphous or crystalline materials, usually showed the formation of patterns which are amorphized in the topmost layers corresponding to the ions penetration depth [38, 41]. Faceting has been reported in the case of irradiation near room temperature of metal surfaces with low melting point and non-directional bonding [38, 42]. More recently faceting has also been reported in the case of elemental semiconductors Ge(001) [43, 44] provided very high sputtering temperatures, above the recrystallization transition, are chosen.

The further possibility to modify via self-organized ion beam sputtering mineral surfaces such as calcite (10.4) face to obtain highly corrugated nanorippled morphologies bound by unusual reactive facets might permit to exploit their enhanced reactivity in water remediation applications. In the following, we describe a controlled experiment in which the morphology of a faceted calcite sample was exposed to a Pb-rich aqueous solution while it was monitored *in situ* and in real time with a AFM equipped with a liquid cell.

The time evolution of the surface morphology as the sorption process goes on is illustrated in the sequence of AFM topography images shown in figure 3. Two stages can be clearly distinguished. In a first stage, the calcite surface morphology resembles that of the original ion-beam induced ripples. Then the interaction of the surface with the lead-bearing aqueous solution leads to a continuous decrease in the surface roughness and to a broadening of the rippled structure. Four hours later (figure 3(d)), the ripple pattern decomposed in several regions and for longer times (5 h, figure 3(e)) most of

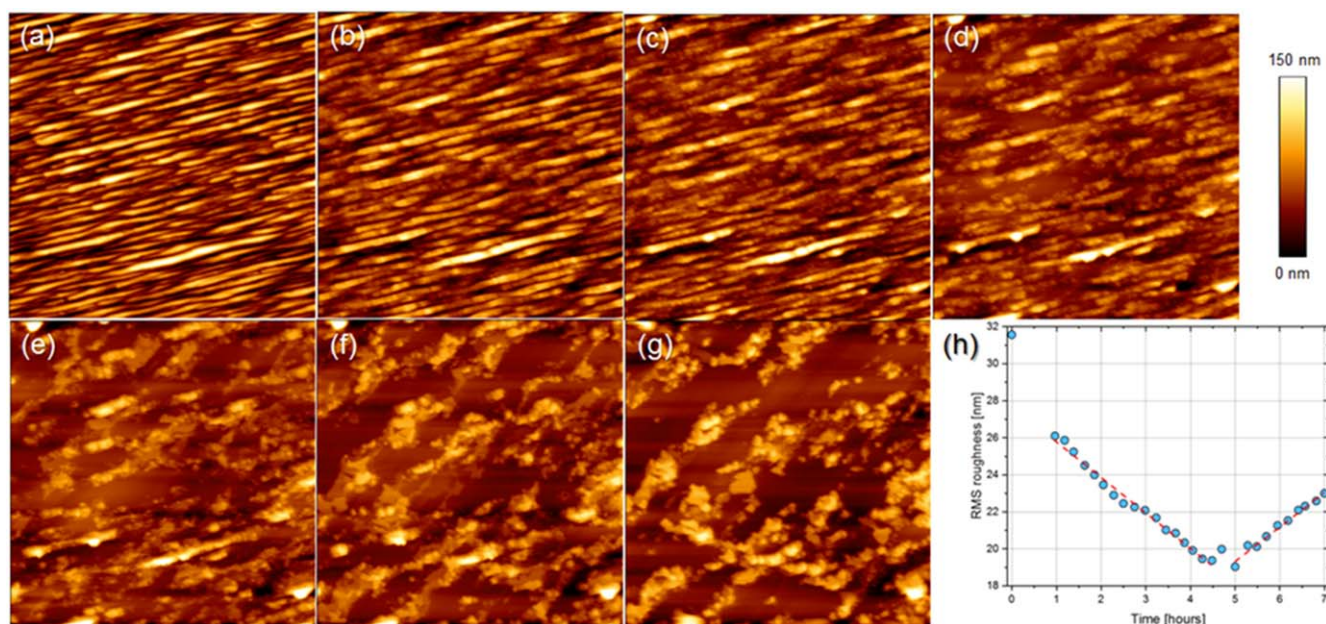


**Figure 3.** (a)–(g) AFM topography images of a rippled calcite (10.4) surface after 1 to 7 h (approximately) in contact with a  $\text{PbCl}_2$  aqueous solution 38.8 mM. Frame sizes:  $10 \times 10 \mu\text{m}^2$ . (h) RMS roughness of the rippled calcite as a function of time of exposure to a  $\text{PbCl}_2$  solution 38.8 mM. A few initial points could not be recorded due to the time required for focusing the laser beam onto the AFM cantilever immersed in the solution.

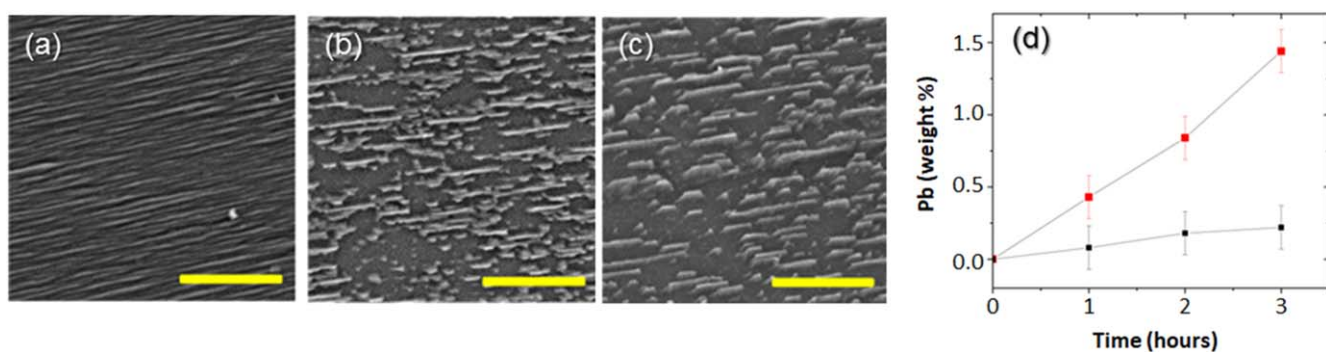


**Figure 4.** SEM topography images (backscattered signal) of the rippled calcite surface after exposure into a bath of  $\text{PbCl}_2$  solution for (a) 1 h, (b) 2 h and (c) 3 h. The yellow scale bars are  $5 \mu\text{m}$  long. (d) Time evolution of the average Pb concentration onto a rippled calcite (10.4) surface (red squares) and onto a reference flat calcite (10.4) surface (black squares).

the pristine ripples were smoothed out. Only sections of the most protruding ridges remained separated by atomically flat areas (figure 3(f)). When the exposure to the Pb-rich solution was further extended, the remains of the original ripples evolved into irregular structures with a pronounced three-dimensional character (figure 3(g)). The variation of the RMS roughness during the first 7 h of the sorption process is shown in figure 3(h). As can be seen in this figure, the RMS roughness decreased down to 20 nm within the first 4.5 h. From this point onwards, the roughness started to increase again. Interestingly, the rates of decrease and increase of RMS roughness have almost the same value ( $1.9 \text{ nm h}^{-1}$ ).

In figures 4(a)–(c) we show representative SEM images of another rippled calcite substrate acquired in the back-scattered electron channel, after exposure to the Pb-rich solution for up to 3 h. The high contrast regions correspond to Pb-bearing precipitates characterized with a higher molecular

mass compared to that of the pristine calcite substrate. After 1 h exposure to the Pb-rich solution (figure 4(a)) the elongation of the Pb precipitates matches quite well the pristine calcite ripple ridges. For longer exposure times (2 h and 3 h, figures 4(b)–(c)), even if the calcite ripples dissolved, the elongated Pb precipitates showed clear evidence of anisotropic coarsening in the direction of the pristine ripple pattern.

To test the Pb sequestration efficiency of the calcite nano-rippled morphology, we have performed chemical analysis of local surface composition using energy dispersive x-ray spectrometry (EDS) (see Methods and SI for details) on different areas of the original sample removed after 1, 2 and 3 h from the aqueous Pb-rich solution. The same was done on freshly-cleaved calcite (10.4) reference faces, which were not exposed to the ion beam nanopatterning process. Remarkably, Pb sequestration rate on the nano-rippled surface increases at approximately 0.5 atomic weight % per hour, i.e. about 500% faster compared to the lead

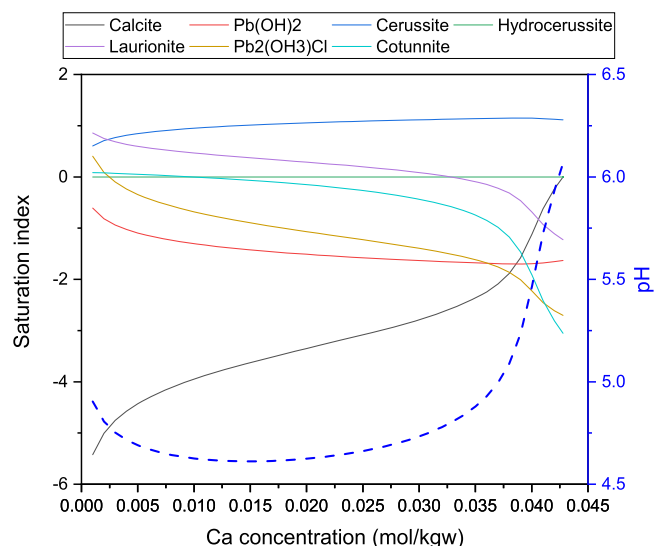


**Figure 5.** Simulation of the evolution of the saturation indexes of Pb-bearing phases and pH as the concentration of Ca increases in the solution due to calcite dissolution. This simulation has been conducted with the code PHREEQC by assuming that the first precipitated phase is hydrocerussite.

uptake rate observed on the calcite (10.4) flat surface (figure 4(d)). We stress that such a high increase in the reaction rate cannot be fully explained by the 60% increase in active surface area of the nanostructured calcite surface with respect to the pristine flat surface reference. The results instead point out to the crucial role played by the highly kinked and reactive stepped (11.0) and (21.12) facet terminations, which are produced during the ion beam sputtering process.

Already in the early stages of the exposure to the Pb-rich solution we occasionally observed some isolated and randomly distributed Pb-bearing 3D-crystallites on top of the rippled pattern (e.g. figure SI 2a recorded after 2 h exposure to the Pb-rich solution). We stress that in the EDS analysis shown in figure 4(d) we avoided to include regions containing those 3D crystallites. As a comparison, the growth of Pb-bearing crystallites on freshly cleaved calcite surfaces proceeds slowly and they are not elongated, as shown in the SEM image of figure SI 2b recorded after 2 h exposure on a flat cleaved surface. In this case, the shallow Pb-bearing crystallites preferentially nucleate along the step edges produced during cleavage. For exposure times to the Pb-rich solution longer than 3 h, once the ripple pattern decomposes, the randomly distributed 3D crystallites become the dominant feature on both flat and rippled calcite substrates. In order to determine accurately the enhancement of Pb uptake associated to the anisotropic distribution of calcite steps in rippled templates, and to avoid artifacts due to the disordered 3D distribution of the Pb-bearing precipitates observed at longer exposure times, the EDS analysis was thus limited to surfaces after a maximum exposure time to the Pb-rich solution of 3 h (figure 4(d)).

To better understand the experimental results observed with AFM and SEM, geochemical modelling was performed using the code PHREEQC, a robust computer program for chemical speciation, widely used to model dissolution and

precipitation processes in geochemical systems involving both aqueous solutions and minerals. In figure 5 we plot the PHREEQC simulations to determine which phases could precipitate from a  $\text{PbCl}_2$  solution in contact with calcite surfaces i.e. the phases with the highest saturation indexes ( $\text{SI}_{\text{phase}}$ ) defined in equation (1) of the methods sections. When  $\text{SI}_{\text{phase}} < 0$  an aqueous solution is undersaturated with respect to the mineral phase, when  $\text{SI}_{\text{phase}} > 0$  such a solution is supersaturated with respect to the mineral phase, and when  $\text{SI}_{\text{phase}} = 0$  the mineral-solution system is at equilibrium. When the Pb-bearing solution was theoretically placed in contact with a calcite surface, the later started to dissolve. As a consequence, the aqueous solution becomes highly supersaturated with respect to hydrocerussite,  $\text{Pb}_3(\text{CO}_3)_2(\text{OH})$ , ( $\text{SI} = 6.55$ ), followed by  $\text{Pb}_2(\text{OH})_3\text{Cl}$  ( $\text{SI} = 4.21$ ) and cerussite,  $\text{PbCO}_3$ , ( $\text{SI} = 2.61$ ) (see equation (1) in the methods section). If dissolution continues until the solution becomes saturated with respect to calcite, the SI for hydrocerussite increases up to 11.13. Differently, if we assume, as shown in figure 4, that hydrocerussite precipitates once it reaches its saturation state ( $\text{SI} = 0$ ), the crystallization of this hydrated lead carbonate leads to a decrease in the pH of the aqueous solution, which further favors the dissolution of calcite. This results in a new increase in the pH of the solution. In such a scenario, when the concentration of Ca is very low at the first stages of dissolution (less than  $1 \text{ mmol kg}^{-1} \text{ w}^{-1}$ ), the most supersaturated phase is laurionite,  $\text{PbCl}(\text{OH})$ . However, when the concentration of Ca in solution increases above  $1 \text{ mmol kg}^{-1} \text{ w}^{-1}$ , cerussite becomes the most supersaturated phase while laurionite and other Pb-bearing phases progressively decrease their SI values. Therefore, we can assume that hydrocerussite followed by cerussite are the two main phases that precipitate in our experiments. Nevertheless, in AFM images only crystals resembling cerussite were detected, probably due to the low adhesion between the hydrocerussite crystals and the calcite surface, which made them easily movable by the AFM tip.

### 3. Conclusions

We have shown a first example of maskless nanofabrication of high-aspect ratio calcite nanopatterns extending homogeneously over a large scale ( $\text{cm}^2$ ) by self-organized Ion Beam Sputtering. Remarkably, the nanorippled calcite (10.4) surfaces, are characterized by singular facet arrays with probable (11.0) and (21.12) terminations. From *in situ* AFM imaging and SEM and EDS analysis, we confirmed that Pb sequestration from an aqueous solution of  $\text{PbCl}_2$  is much faster on calcite nanostructured substrates than on flat ones. A remarkable 500% increase in the Pb up take rate leads to the formation of elongated Pb-bearing precipitates, which oriented parallel to the original calcite rippled nanopattern. The high reactivity of the kinked (11.0) and (21.12) calcite facets seems to be responsible for the strong enhancement of Pb up take rate compared to a flat calcite (10.4) reference face. Geochemical modelling are consistent with the experimental observations, and they indicate that hydrocerussite followed

by cerussite are the main lead minerals formed on calcite surfaces. The superior performance of these novel nanostructured calcite surfaces in promoting sequestration of heavy metal ions (i.e. Pb) paves the way towards the fabrication of large scale porous membranes for water purification and environmental applications.

#### 4. Methods

**Ion beam sputtering.** A flat calcite slab ( $20 \times 15 \times 3 \text{ mm}^3$ ) is rinsed in de-ionized water and dried with a N<sub>2</sub> gas flux. The sample is then placed in a custom-made vacuum chamber equipped with a TECTRA ion gun and irradiated at room temperature with a low energy defocused 800 eV Ar<sup>+</sup> ion beam at  $4 \times 10^{-4}$  mbar of pressure (gas purity N5.0). Positive charge build-up on the sample surface is avoided by a biased tungsten filament through electron thermionic emission. The ion beam irradiates the calcite sample at an incident angle of  $\theta = 80^\circ$  with respect to its surface normal. The ion fluency is equal to  $5.9 \times 10^{18}$  ions  $\text{cm}^{-2}$ .

**Reacting solution.** The concentration of the initial solution used in the experiments and the dissolution of the calcite substrate in contact with such a solution was simulated using the PHREEQC code for chemical speciation [45]. The saturation indexes for the different lead phases ( $SI_{\text{phase}}$ ) in the solution were calculated using the PHREEQC code, the PHREEQC.dat database, the Tipping\_Hurley.dat database for solubility products of lead phases and the following general expression:

$$SI_{\text{phase}} = \log \left( \frac{IAP}{K_{\text{sp}}} \right), \quad (1)$$

where IAP is the ion activity product of the dissolved ions and  $K_{\text{sp}}$  is the solubility product of the considered mineral phases.

For the reacting solution, a slightly supersaturated solution with respect to PbCl<sub>2</sub> was chosen, i.e.  $SI = 0.09$ . Using PHREEQC and equation (1) the concentration of the solution used in the experiments was 38.8 mM at 20 °C. The solution was prepared using PbCl<sub>2</sub> powder and deionized water (Milli-Q, resistivity 18 MΩ cm).

**Atomic force microscopy (AFM).** The topography images of the calcite surfaces immersed in the PbCl<sub>2</sub> aqueous solution were acquired with a NanoWizard 4 AFM (JPK Instruments, Berlin) operated in contact mode with ContAIG probes (<10 nm tip radius; 13 kHz frequency by Budget-Sensors) at 10 nN with a line rate of 1 Hz.

**Scanning electron microscopy (SEM).** Top view back-scattered electrons images were acquired with a variable-pressure Hitachi VP-SEM SU3500 thermionic scanning electron microscope, operating in the 10 kV accelerating voltage range and 20–30 Pa pressure range to avoid surface charging on the insulating substrate.

**Energy dispersive x-ray spectrometry (EDS).** EDS measurements were performed by means of the Hitachi VP-SEM SU3500 equipped with a Thermo Scientific Noran System 7 Compact EDS module. EDS spectra were collected and analyzed with Thermo Scientific NSS 3 x-ray Microanalysis software. EDS

spectra (see SI) were acquired with a primary electron beam energy of 10 kV at 40 Pa of pressure by scanning a sample area of  $2.83 \times 10^{-3} \text{ mm}^2$ . Several spectra were collected for each considered sample and averaged to obtain the Pb weight percentages reported in figure 4(b). Note that, since the EDS samples about 0.5 μm spots, single ripples could not be resolved.

**Calcite structure study.** The in-depth calcite structure study was performed using VESTA software [46]. Different planes with inclinations approximating the AFM measurements were simulated for the ripples, considering the face (10.4) as the horizontal surface from which the ripples are generated. The calcite structure used for this study is the one defined by Maslen *et al* [47].


#### Acknowledgments

SC thanks Universidad Técnica de Ambato (UTA), Dirección de Investigación y Desarrollo (DIDE), and Freddy Del Pozo for their help and management. CP acknowledges a Juan de la Cierva-Formación postdoctoral contract (ref. FJC2018–035820-I) from the Spanish Ministry of Science. MCG and FBdM acknowledge support by MAECI in the framework of the Italy-Vietnam bilateral program ‘Progetti di Grande Rilevanza 2021–2023’, by Ministero dell’Università e della Ricerca (MUR), Project funded under the National Recovery and Resilience Plan (NRRP), Mission 4 Component 2 Investment 1.3 - Call for tender No. 1561 of 11.10.2022; funded by the European Union – NextGenerationEU • Award Number: Project code PE0000021, Concession Decree No. 1561 of 11.10.2022 adopted by Ministero dell’Università e della Ricerca (MUR), CUP D33C22001300002 Project title “Network 4 Energy Sustainable Transition – NEST”. FBdM acknowledges support by UNIGE in the framework of BIPE2020 program and technical support from R Chittofrati and E Vigo.

#### Data availability statement

The data cannot be made publicly available upon publication because they are not available in a format that is sufficiently accessible or reusable by other researchers. The data that support the findings of this study are available upon reasonable request from the authors.

#### ORCID iDs

Francesco Buatier de Mongeot  <https://orcid.org/0000-0002-8144-701X>

Enrico Gnecco  <https://orcid.org/0000-0002-3053-923X>

#### References

- [1] Stewart B A, Lal R and Stewart B A 2020 *Soil Processes and Water Quality* 1st edn (Boca Raton, FL: CRC Press)

- [2] Lee M, Paik I S, Kim I, Kang H and Lee S 2007 *J. Hazard. Mater.* **144** 208–14
- [3] Simeonidis K, Kaprara E, Samaras T, Angelakeris M, Pliatsikas N, Vourlias G, Mitrakas M and Andritsos N 2015 *Sci. Total Environ.* **535** 61–8
- [4] Hilal Elhousseini M, Isik T, Kap Ö, Verpoort F and Horzum N 2020 *Appl. Surf. Sci.* **514** 145939
- [5] Agwarambo L, Magee N, Nunez S and Mitt K 2013 *J. Environ. Prot.* **04** 1251–7
- [6] Fukushi K, Munemoto T, Sakai M and Yagi S 2011 *Sci. Technol. Adv. Mater.* **12** 064702
- [7] Knox A S, Kaplan D I, Adriano D C, Hinton T G and Wilson M D 2003 *J. Environ. Qual.* **32** 515–25
- [8] Garrido F, Illera V and García-González M T 2005 *Appl. Geochem.* **20** 397–408
- [9] Rodríguez-Jordá M P, Garrido F and García-González M T 2010 *J. Hazard. Mater.* **175** 762–9
- [10] Xu Y, Liang X, Xu Y, Qin X, Huang Q, Wang L and Sun Y 2017 *Pedosphere* **27** 193–204
- [11] Otunola B O and Ololade O O 2020 *Environ. Technol. Innov.* **18** 100692
- [12] Gu S, Kang X, Wang L, Lichtfouse E and Wang C 2019 *Environ. Chem. Lett.* **17** 629–54
- [13] Liang X, Han J, Xu Y, Wang L, Sun Y and Tan X 2014 *Appl. Surf. Sci.* **322** 194–201
- [14] Grommet A B, Feller M and Klajn R 2020 *Nat. Nanotechnol.* **15** 256–71
- [15] Qu X, Zhao B, Zhang W, Zou J, Wang Z, Zhang Y and Niu L 2022 *J. Phys. Chem. Lett.* **13** 830–7
- [16] Larmier K, Tada S, Comas-Vives A and Copéret C 2016 *J. Phys. Chem. Lett.* **7** 3259–63
- [17] Goronzy D P et al 2018 *ACS Nano* **12** 7445–81
- [18] Buatier de Mongeot F and Valbusa U 2009 *J. Phys. Condens. Matter* **21** 224022
- [19] Michalak D J, Amy S R, Aureau D, Dai M, Estève A and Chabal Y J 2010 *Nat. Mater.* **9** 266–71
- [20] Liu D, Li L, Gao Y, Wang C, Jiang J and Xiong Y 2015 *Angew. Chem. Int. Ed.* **54** 2980–5
- [21] Giordano M C and de Mongeot F B 2018 *Adv. Mater.* **30** 1801840
- [22] Gnecco E, Nita P, Casado S, Pimentel C, Mougin K, Giordano M C, Repetto D and Mongeot F B de 2014 *Nanotechnology* **25** 485302
- [23] Kim H Y and Henkelman G 2013 *J. Phys. Chem. Lett.* **4** 216–21
- [24] Barelli M, Mazzanti A, Giordano M C, Della Valle G and Buatier de Mongeot F 2020 *Nano Lett.* **20** 4121–8
- [25] Giordano M C, Tzschoppe M, Barelli M, Vogt J, Huck C, Canepa F, Pucci A and Buatier de Mongeot F 2020 *ACS Appl. Mater. Interfaces* **12** 11155–62
- [26] Giordano M C, Repetto D, Mennucci C, Carrara A and Mongeot F B de 2016 *Nanotechnology* **27** 495201
- [27] Mennucci C, Muhammad M H, Hameed M F O, Mohamed S A, Abdelkhalik M S, Obayya S S A and Buatier de Mongeot F 2018 *Appl. Surf. Sci.* **446** 74–82
- [28] Adetunji J and Barber D J 1978 *J. Mater. Sci.* **13** 627–38
- [29] Prieto M, Heberling F, Rodríguez-Galán R M and Brandt F 2016 Crystallization behavior of solid solutions from aqueous solutions: an environmental perspective *Progress Cryst. Growth Charact. Mater.* **62** 29–68
- [30] Pina C M and Jordan G 2010 Reactivity of mineral surfaces at nano-scale: kinetics and mechanisms of growth and dissolution in nanoscopic approaches in earth and planetary sciences *Mineralogical Society of Great Britain and Ireland ed G Ferraris et al* (London) pp 239–323
- [31] Hochella M F and White A F (ed) 1990 *Mineral-Water Interface Geochemistry* (Berlin: De Gruyter)
- [32] Vaughan D J 1995 Mineral surfaces *The Mineralogical Society Series* 1st edn (Boca Raton, FL: Chapman & Hall)
- [33] Godelitsas A, Astilleros J M, Hallam K, Harissopoulos S and Putnis A 2003 *Environ. Sci. Technol.* **37** 3351–60
- [34] Callagon E, Fenter P, Nagy K L and Sturchio N C 2014 *Environ. Sci. Technol.* **48** 9263–9
- [35] Yuan K, Lee S S, De Andrade V, Sturchio N C and Fenter P 2016 *Environ. Sci. Technol.* **50** 12984–91
- [36] Pimentel C, Gnecco E and Pina C M 2018 *J. Phys. Chem. C* **122** 22487–93
- [37] Pimentel C, Mougin K, Gnecco E and Pina C M 2020 *J. Cryst. Growth* **550** 125892
- [38] Valbusa U, Boragno C and Mongeot F B de 2002 *J. Phys. Condens. Matter* **14** 8153–75
- [39] de Mongeot F B, Toma A, Molle A, Lizzit S, Petaccia L and Baraldi A 2006 *Phys. Rev. Lett.* **97** 056103
- [40] Helveg S, Lauritsen J V, Lægsgaard E, Stensgaard I, Nørskov J K, Clausen B S, Topsøe H and Besenbacher F 2000 *Phys. Rev. Lett.* **84** 951–4
- [41] Giordano M C, Sacco F, di, Barelli M, Portale G and Buatier de Mongeot F 2021 *ACS Appl. Nano Mater.* **4** 1940–50
- [42] Molle A, de Mongeot F B, Molinari A, Xiaerding F, Boragno C and Valbusa U 2004 *Phys. Rev. Lett.* **93** 256103
- [43] Ou X, Keller A, Helm M, Fassbender J and Facsko S 2013 *Phys. Rev. Lett.* **111** 016101
- [44] Engler M and Michely 2016 *Phys. Rev. B* **93** 085423
- [45] Parkhurst D L and Appelo C A J 2013 Description of Input and Examples for PHREEQC Version 3—A Computer Program for Speciation, Batch–Reaction, One–Dimensional Transport, and Inverse Geochemical Calculations. U.S. Geological Survey Techniques and Methods 6, chap. A43. vol chap. A43 (USGS)
- [46] Momma K and Izumi F 2011 *J. Appl. Crystallogr.* **44** 1272–6
- [47] Maslen E N, Streltsov V A, Streltsova N R and Ishizawa N 1995 *Acta Crystallogr. B* **51** 929–39